Nanoscale

RSC Publishing

PAPER

View Article Online
View Journal | View Issue

Cite this: *Nanoscale*, 2013, **5**, 4449

Strong magnetic enhancement in self-assembled multiferroic-ferrimagnetic nanostructures†

Ying-Jiun Chen,[a] Ying-Hui Hsieh,[b] Sheng-Chieh Liao,[c] Zhiwei Hu,[de] Meng-Jie Huang,[a] Wei-Cheng Kuo,[f] Yi-Ying Chin,[a] Tzeng-Ming Uen,[f] Jenh-Yih Juang,[f] Chih-Huang Lai,[c] Hong-Ji Lin,*[a] Chien-Te Chen[a] and Ying-Hao Chu*[b]

Received 7th January 2013
Accepted 18th March 2013

DOI: 10.1039/c3nr00104k

www.rsc.org/nanoscale

In the past decade, self-assembled vertical nano-heterostructures have drawn considerable attention because a high interface-to-volume ratio can be used to tailor or create functionalities. We have systematically investigated the magnetic properties of oxide heterostructures consisting of the $CoFe_2O_4$ nanopillars embedded in the $BiFeO_3$ matrix using macroscopic magnetization measurements and element-selective soft X-ray absorption magnetic circular dichroism (XMCD) at the Co- and Fe-$L_{2,3}$ edge. The magnetization and XMCD data show that the total ordered magnetic moment of Co^{2+} in $CoFe_2O_4$–$BiFeO_3$ nano-heterostructures is strongly enhanced. This study clearly indicates that the high interface-to-volume ratio vertical nanostructure creates a strong ferromagnetic and antiferromagnetic magnetic coupling *via* an interface. Furthermore, the magnetic coupling can be tuned in the multiferroic-ferrimagnetic self-assembled heterostructures by controlling the spacing between nanopillars.

Introduction

The interplay between lattice, charge, orbital, and spin degrees of freedom in complex oxides covers a broad spectrum of intriguing functionalities.[1] Heterostructures containing complex oxides provide a powerful route to manipulate these degrees of freedom and offer tremendous opportunities for next-generation electronic devices.[2,3] One good example is to build up oxide heterostructures for energy efficient nonvolatile memory and logic spintronic devices *via* electric-field control of magnetism.[4,5] In this category, two pathways have been successfully demonstrated. The first one is based on piezoelectric-ferromagnet heterostructures *via* strain mediated coupling between piezoelectricity and magnetostriction to achieve the electric-field control of magnetic anisotropy and magnetization.[6,7] The other promising structure is in the use of ferromagnet-multiferroic nanostructures to demonstrate the electric-field control of the magnetization rotation.[8,9] The key to this success is the coupling through the interfaces in the heterostructures. In the past decade, in order to tailor or create the functionalities, one specific type of heterostructure drawing extensive attention is the high interface-to-volume ratio vertical nanostructure.[10] The same concept has been applied to build up piezoelectric and magnetostrictive self-assembled heterostructures, such as $BaTiO_3$–Co_2FeO_4 (CFO) and $BiFeO_3$ (BFO)–CFO to show enhanced magnetoelectric effects.[11,12] However, the idea of using multiferroic and ferri/ferromagnet nanostructures is yet to be addressed. One important question arises: how to understand the magnetic coupling between matrix and nanopillars in this type of self-assembled heterostructures? In order to explore this possibility, we adapted a model system and study the magnetic coupling behaviors systematically.

Spinel ferrite CFO exhibits a large spin polarization, high ferrimagnetic order temperature (T_C = 793 K), large magnetocrystalline anisotropy and magnetostriction, unique nonlinear spin wave properties and considerable saturation magnetizations, while BFO shows very large spontaneous polarization with high ferroelectric Curie temperature ($T_C \sim$ 1100 K) and high antiferromagnetic (AFM) temperature ($T_N \sim$ 640 K).[13,14] In this work, we investigated the magnetic properties of the ordered CFO nanopillars embedded in the BFO matrix by means of magnetization experiments and element-selective X-ray magnetic circular dichroism (XMCD) to understand the magnetic coupling in this type of heterostructures. We found a significant enhancement of the ordered magnetic moment of Co^{2+} ions for the CFO nanopillar-embedded BFO matrix as compared with those of the $SrTiO_3$ (STO) matrix and CFO–BFO

[a]*National Synchrotron Radiation Research Center, Hsinchu 30076, Taiwan. E-mail: hjlin@nsrrc.org.tw*

[b]*Department of Materials Science and Engineering, National Chiao Tung University, Hsinchu 30010, Taiwan. E-mail: yhc@nctu.edu.tw*

[c]*Department of Materials Science and Engineering, National Tsing Hua University, Hsinchu 30013, Taiwan*

[d]*Physikalisches Institut, Universität zu Köln, Zülpicher Strasse 77, D-50937 Köln, Germany*

[e]*Max Planck Institute for Chemical Physics of Solids, Nöthnitzerstrasse 40, D-01187 Dresden, Germany*

[f]*Department of Electrophysics, National Chiao Tung University, Hsinchu 30100, Taiwan*

† Electronic supplementary information (ESI) available. See DOI: 10.1039/c3nr00104k

bilayer thin film. Controlling the spacing between the CFO nanopillars further provides a pathway to tune the coupling at the ferrimagnetic/multiferroic interfaces as well as the magnetization of the BFO–CFO nanostructures. This study suggests that mastering the unconventional mechanisms at intriguing oxide interfaces is vital to engineer interlinks among ferroic orders and the spin by such exotic heterostructures. This certainly helps with the continuing pursuit for practical room-temperature multiferroic materials for high-performance oxide-based devices.

Results and discussion

100 nm BFO–CFO on STO (001) self-assembled nanostructures were prepared by pulsed laser deposition (PLD) assisted with high-pressure reflective high-energy electron diffraction (RHEED) at 700 °C in O_2 (200 mTorr).[15] In addition, in order to gain the flexibility to manipulate the composition of oxide thin films, combinatorial deposition was employed.[16,17] Two ceramic discs (one CFO and one BFO) were used as the targets that fed the substrates separately. These two targets were mounted on an exchanging stage automated by an external motor and were shot by laser pulses alternately during the deposition. The end product of the deposition was a BFO–CFO composite thin film with volume fractions ranging from pure CFO to pure BFO controlled by the number of laser pulses received by each target. To avoid the formation of multilayered structures, the number of laser pulses shot on the CFO and BFO targets was further controlled so that neither of the two materials grew more than one unit cell in thickness in each alternation cycle. The quality of the samples has been characterized by various techniques.[15] Reference samples such as STO–CFO nanostructures and CFO–BFO bilayer structures were also fabricated using the same growth method. The CFO–STO sample is a reference to prove that antiferromagnetism of the matrix is key to driving this magnetic interaction. The thickness of the CFO and BFO layer in a bilayer sample was kept as the same volume as the sample of CFO–BFO nanostructures. Typically, spinel nanostructures form nanopillars (~60 nm) embedded in a perovskite matrix owing to the surface energy anisotropy.[18] Fig. 1(a) and (b) show respectively the schematic of BFO perovskite–CFO spinel nanostructures on STO (001) and the topography image of the obtained nanostructures taken using an atomic force microscope. A very good separation of nanopillars was observed. Fig. 1(c) is a reciprocal space mapping (RSM) taken by X-ray diffraction technique, and it clearly shows the phase separation, good crystallinity, and the epitaxial relationships among the nanopillars, matrix, and substrate. Such a nanostructure provides us a good template to further probe the magnetic coupling between antiferromagnetic BFO matrix and ferromagnetic CFO nanopillars.

Strong magnetic interactions have been observed in various antiferromagnetic/ferromagnetic heterostructures.[19–21] Two typical behaviors have been observed; one is the exchange-bias and the other is the strong exchange enhancement. In order to explore the coupling behaviors, the macroscopic magnetic characterization was carried out by superconducting quantum interference device (SQUID) magnetometry. Fig. 2 shows the out-of-plane magnetization hysteresis (*M–H*) loops for the samples at room temperature with both ±5 T magnetic field aligned along the [001] direction. A diamagnetic substrate contribution from the STO substrate is corrected by subtracting the curves of the bare substrates from the raw magnetic data. We observed a notably strong enhancement of the saturation magnetization in the BFO–CFO nanostructure compared to the STO–CFO (CFO lateral size is about 30 nm) nanostructure and the CFO–BFO bilayer. The data captured from the SQUID measurements suggest a strong magnetic enhancement between the BFO matrix and CFO nanopillars.

In order to delineate the origin of the magnetic coupling, we have employed X-ray absorption spectroscopy (XAS) and X-ray magnetic circular dichroism (XMCD). These techniques supply an extremely sensitive local probe for element-specific magnetometry and are ideal tools to study the valence states, spin characters as well as the orbital contribution to the magnetic moment. The Co- and Fe-$L_{2,3}$ XAS and XMCD spectra were recorded at the Dragon beamline of the National Synchrotron Radiation Research Center (NSRRC) in Taiwan with an energy resolution of 0.25 eV. The sharp peak at 777.1 eV of the Co-L_3 edge of single crystalline CoO and at 709.4 eV of the Fe-L_3 of single crystalline Fe_2O_3 were used for energy calibration, which

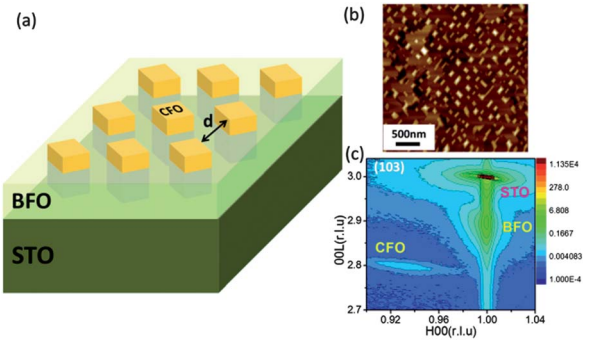

Fig. 1 (a) Schematic of perovskite–spinel self-assembled vertical heterostructures. Perovskite materials from matrix and pillars are spinel on STO (001). (b) AFM topography image and (c) the X-ray RSM of (113) reflection of the BFO–CFO self-assemble system. A clear phase separation is observed.

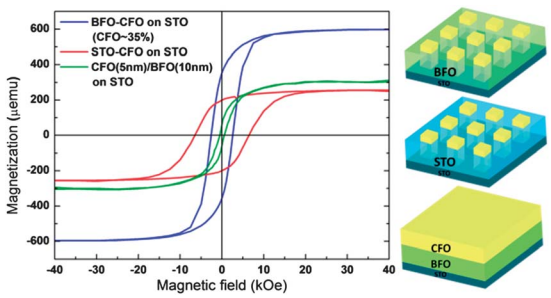

Fig. 2 Magnetic hysteresis loops of BFO–CFO, STO–CFO vertical heterostructures and CFO–BFO bilayer on the STO substrate along the out-of-plane direction at room temperature. A large magnetic moment is found in BFO–CFO vertical heterostructures compared with others.

enabled us to achieve better than 0.05 eV accuracy in the relative energy alignment. The XMCD spectra at both the Co-$L_{2,3}$ and the Fe-$L_{2,3}$ edges were measured at room temperature in a 1 T magnetic field with approximately 80% circularly polarized light. The magnetic field makes an angle of 30° with respect to the Poynting vector of the soft X-rays. The spectra were recorded using the total electron yield method (by measuring the sample drain current) in a chamber with a base pressure of 1×10^{-9} mbar. The unique features exhibited in the XMCD spectrum at the 3d transition metal $L_{2,3}$ edges are excellent probes for investigating spin and orbital moments separately on the individual 3d transition metals. Fig. 3 depicts Co-$L_{2,3}$ (3a) and Fe-$L_{2,3}$ (3b) XAS spectra of CFO–BFO taken by using circularly polarized light with the photon spin parallel (μ^+) and antiparallel (μ^-) to the magnetic field. The spectral line-shape and energy position of μ^+ and μ^- at the Co-$L_{2,3}$ edge of CFO–BFO in Fig. 3(a) is very similar to what was observed in $LaCo_{0.5}Mn_{0.5}O_3$, indicating Co^{2+} valence states at the octahedral (B) sites.[22] Two sharp peaks at the Fe-L_3 edge lie at the same energy as the reference Fe_2O_3 single crystal, demonstrating Fe^{3+} valence states (Fig. 3(b)). There are no spectral features at 705 eV at the Fe-L_3 edge and 718 eV at the Fe-L_2 edge observed in $Co_{1-x}Fe_{2+x}O_4$/MgO thin films.[23] This suggests that the CFO–BFO sample is free from Fe^{2+} ions. XAS data clearly indicate that no chemical reaction occurred in the nanostructures. Note that the different sites of Fe^{3+} ions become much more evident in XMCD. The positive and negative peaks correspond to the directions of the spins of the Fe^{3+} ions at the tetrahedral and octahedral sites, respectively which are coupled antiferromagnetically while the negative peaks of Co^{2+} and Fe^{3+} at the octahedral sites are parallel but are antiparallel to Fe^{3+} at tetrahedral sites (see ESI Fig. S1†).

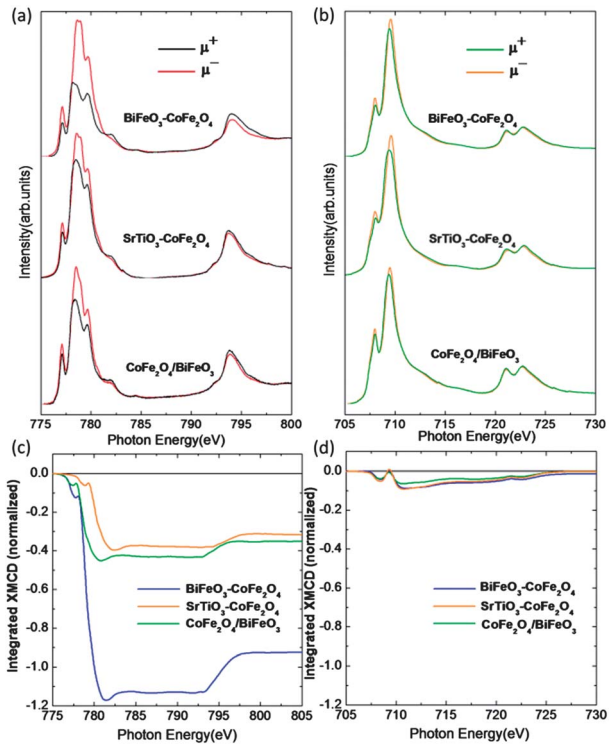

Fig. 3 (a) Co- and (b) Fe-$L_{2,3}$ spectra of $BiFeO_3$–$CoFe_2O_4$ heterostructures on an STO substrate taken with circularly polarized X-rays. The photon spin was aligned parallel (μ^+) or antiparallel (μ^-) to the 1 tesla magnetic field, respectively. Integrated values of the (c) Co- and (d) Fe-normalized XMCD spectra. The blue, orange and green curves correspond to the $BiFeO_3$–$CoFe_2O_4$, $SrTiO_3$–$CoFe_2O_4$ and $BiFeO_3$–$CoFe_2O_4$ bilayers on the STO substrate, respectively.

A considerably large XMCD signal at the Co edge in BFO–CFO was observed as compared with that in STO–CFO heterointerfaces and in the BFO–CFO bilayer (Fig. 3(a)). We have obtained 52% XMCD signal at the Co-L_3 edge in BFO–CFO. This is much larger than 19% in the STO–CFO heterostructure and 3% in CFO–MgO (see ESI Fig. S1†).[23] To determine the magnetic coupling quantitatively, we used the XMCD sum rules to separate the orbital (M_{orb}) and spin (M_{spin}) contributions to the total ferromagnetic moment for the Co and Fe cations. The integrals of the Fe XMCD spectra in Fig. 3(d) show that the orbital moment is essentially quenched as expected, while there is a significant orbital component to the magnetic moment of the Co (Fig. 3(c)). Furthermore, the Fe net spin moments (~0.19 μ_B) are much smaller than cobalt ones for all three samples. In $CoFe_2O_4$, the Fe^{3+} ions at octahedral and tetrahedral sites have an antiferromagnetic alignment. Therefore, they do not contribute to the net spin moment. This is consistent with our sum rule calculations and reveals that the majority of the magnetic moment for all the systems is owing to the Co^{2+} cations.[23] Note that the value of the Co out-of-plane total moment is estimated as large as 2.39 μ_B (2.46 μ_B in-plane) for the BFO–CFO and 0.93 μ_B for the STO–CFO. These are larger than that in the bulk Co metal[24] and seldom known in the oxide-based magnetic materials. A detailed analysis of the values of the orbital and spin moments is described in the ESI.†

One possible mechanism that could give rise to strong magnetic coupling in BFO–CFO heterostructures is the epitaxial strain of CFO nanopillars imposed by either the substrate or matrix. However, this can be excluded because the lattice mismatch between CFO and perovskites (STO and BFO) is extremely large (~7%). Consequently, the spinel–perovskite interfaces have been largely relaxed by the formation of misfit dislocations, which, in turn, resulted in semicoherent interfaces.[25] In addition, the lattice parameters derived from the XRD curve for CFO (004)c on STO, BFO–CFO and STO–CFO are very close to bulk CFO, suggesting that CFO nanopillars embedded in perovskite matrices are not strained.[15] Moreover, $CoFe_2O_4$ thin films grown on higher symmetry substrates, such as MgO and $SrTiO_3$, show a reduced saturation magnetization of 25–60% of the bulk value.[23,26] Moyer *et al.* found merely ~2.6% XMCD signal at the Co-L_3 edge of CFO thin films grown epitaxially on MgO (001) substrates.[23] Comparing the BFO–CFO with STO–CFO heterostructures, SQUID and XMCD show that the total magnetic moment of BFO–CFO is about 3 times larger than that of STO–CFO under a 1 T magnetic field. No enhancement of the FM signal for Co^{2+} ions in the STO–CFO heterostructures and CFO–BFO bilayer indicates that the antiferromagnetism of the BFO matrix might have a strong influence on the CFO nanopillars. This directly suggests that the gigantic enhancement of the magnetization may be due to an interface-mediated enhancement of magnetic coupling in the

BFO–CFO heterostructures. The interfacial exchange energy dominates over other energies in the system due to a large surface-to-volume ratio in the heterostructures. It is very known that there are uncompensated AFM spins at the FM and AFM interface. If the interfacial uncompensated spins are pinned in the AFM, exchange bias is expected. On the other hand, if uncompensated spins are rotatable with the FM, there is no exchange bias.[27–30] Antel *et al.* showed an uncompensated surface with a net FM moment of almost one atomic layer at the interface.[27] The uncompensated Fe^{3+} spin can be aligned along the external magnetic field because the closed spin-up shell of a high spin $3d^5$ configuration does not have orbital moment and has a weak magnetic anisotropic energy. No observation of exchange bias indicates that the uncompensated spin is rotatable.[28–30] The FM alignment of the uncompensated Fe^{3+} spin from BFO at the interface provides an additional exchange field acting on the Co^{2+} together with the exchange field from B-site Fe^{3+} ions in CFO as shown in Fig. 4(b). In the following, the interaction between Co^{2+} ions from different layers of a CFO nanopillar should contribute to the total magnetization due to the strong ferromagnetic coupling between the layers. However, the B-site Fe^{3+} ions are partly canceled by A-site Fe^{3+} ions due to the antiparallel arrangement between them. The interfacial uncompensated spins have been ubiquitously identified in an FM Co metal cluster covered with AFM CoO shell.[19,21,31] It is found that the magnetization does not change when the CFO nanopillars are embedded in the STO matrix. We propose that the enhanced magnetic performance of CFO nanopillars is attributed to the strong magnetic coupling in the multiferroic-ferrimagnetic state. Thus, for feasible applications in multifunctional devices only multiferroic orders at room temperature might not be sufficient, and perhaps of the most importance is to acquire a strong coupling interaction between the ferroic orders.

In order to verify the proposed model and qualitatively understand the interfacial coupling strength between CFO nanopillars and the BFO matrix, we have studied the ordered moments as a function of the CFO volume fraction at room temperature using element-selective XMCD and SQUID measurements. The results are presented in Fig. 5 in which the green curve corresponds to the normalized XMCD signal at the Co-L_3 edge and Co total magnetic moment, respectively. We have observed a critical CFO volume fraction of the 65% for CFO nanopillars. Across this point, the ordered moments of Co ions have a sharp change by a factor of three. The AFM moments near the interface decrease as the spacing between CFO nanopillars is smaller than about 10 nm. It was found previously that there is a critical BFO thickness of about 10 nm, below which the net magnetization in BFO disappears in the CoFeB–BFO bilayer system.[32,33] Therefore, the vertical thickness of BFO contributed to maximization of exchange coupling at the interface, *i.e.*, $t_{(BFO)} > 10$ nm. The interfacial exchange coupling would be stronger for the larger spacing between CFO nanopillars. This result provides a control over the average volume fractions of the vertical BFO–CFO nanostructures and the possibility of manipulating multiferroic properties *via* tuning the spacing between CFO nanopillar arrays.

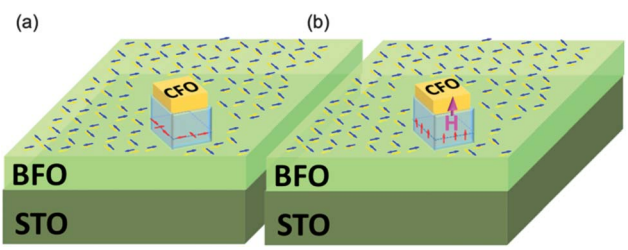

Fig. 4 Schematic rotatable uncompensated AFM BFO spin (red arrow) at the BFO–CFO interface: (a) without external magnetic field; (b) with external magnetic field (*H*).

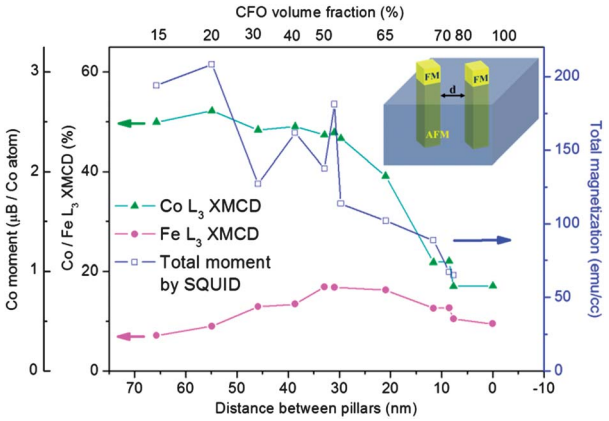

Fig. 5 Magnetism at the spatial limit. Normalized XMCD intensity at the Fe-L_3 edge, Co-L_3 edge and Co total magnetic moment as a function of the distance between pillars at room temperature, $B = 1$ T. The total magnetic moment determined by SQUID magnetometry also agrees with XMCD results.

Methods

BFO–CFO nanostructures, STO–CFO nanostructures and CFO–BFO bilayers used in this study were fabricated by pulsed laser deposition (PLD) with a 248 nm KrF laser, assisted with high pressure reflective high energy electron diffraction (RHEED). The samples were grown at 700 °C in O_2 (200 mTorr). The composition-variation BFO–CFO nanostructures are fabricated by two-target alternating deposition. Reciprocal space mapping (RSM) was taken with 8-circle diffractometer at BL17B in National Synchrotron Radiation Research Center (NSRRC). Topography studies were performed using Veeco EnviroScope operating in tapping mode. Magnetic hysteresis loop is taken with Princeton Measurement Corporation Model 3900 VSM and Quantum Design MPMS-XL SQUID. The Co- and Fe-$L_{2,3}$ XAS and XMCD spectra were recorded at the Dragon beamline in NSRRC in Taiwan.

Conclusions

To summarize, the dramatic enhancement of magnetic moments in BFO–CFO heterostructures suggests a strong magnetic coupling between nanopillars and matrix in the self-assembled nanostructures. We also demonstrated the tunable

local magnetic coupling strength in multiferroic-ferrimagnetic self-assembled heterostructures by controlling the spacing between nanopillars. This work provides a systematic guideline for the optimization of their local coupling strength, consequently yielding a control over the magnetoelectric effect. The realization of coupling between ferroic orders in such vertical heterostructures promises to achieve excellent room-temperature multiferroic heterostructures for next-generation low-energy consumption spintronics.

Acknowledgements

The work was supported by the National Science Council of Republic of China (under contract no. NSC-101-2119-M-009-003-MY2), Ministry of Education (grant no. MOE-ATU 101W961), and Center for Interdisciplinary Science at National Chiao Tung University.

Notes and references

1 H. Takagi and H. Y. Hwang, *Science*, 2010, **327**, 1601–1602.
2 J. Mannhart and D. G. Schlom, *Science*, 2010, **327**, 1607–1611.
3 H. Y. Hwang, Y. Iwasa, M. Kawasaki, B. Keimer, N. Nagaosa and Y. Tokura, *Nat. Mater.*, 2012, **11**, 103–113.
4 R. Ramesh and N. A. Spaldin, *Nat. Mater.*, 2007, **6**, 21–29.
5 M. Bibes and A. Barthelemy, *Nat. Mater.*, 2008, **7**, 425–426.
6 M. Grzelczak, J. Vermant, E. M. Furst and L. M. Liz-Marzán, *ACS Nano*, 2010, **4**, 3591.
7 S. Zhang, Y. G. Zhao, P. S. Li, J. J. Yang, S. Rizwan, J. X. Zhang, J. Seidel, T. L. Qu, Y. J. Yang, Z. L. Luo, Q. He, T. Zou, Q. P. Chen, J. W. Wang, L. F. Yang, Y. Sun, Y. Z. Wu, X. Xiao, X. F. Jin, J. Huang, C. Gao, X. F. Jin and R. Ramesh, *Phys. Rev. Lett.*, 2012, **108**, 137203.
8 Y. H. Chu, L. W. Martin, M. B. Holcomb, M. Gajek, S. J. Han, Q. He, N. Balke, C. H. Yang, D. Lee, W. Hu, Q. Zhan, P. L. Yang, A. Fraile-Rodriguez, A. Scholl, S. X. Wang and R. Ramesh, *Nat. Mater.*, 2008, **7**, 478–482.
9 J. T. Heron, M. Trassin, K. Ashraf, M. Gajek, Q. He, S. Y. Yang, D. E. Nikonov, Y. H. Chu, S. Salahuddi and R. Ramesh, *Phys. Rev. Lett.*, 2011, **107**, 217202.
10 J. L. Mac-Manus-Driscoll, *Adv. Funct. Mater.*, 2010, **20**, 2035–2045.
11 H. Zheng, J. Wang, S. E. Lofland, Z. Ma, L. Mohaddes-Ardabili, T. Zhao, L. Salamanca-Riba, S. R. Shinde, S. B. Ogale, F. Bai, D. Viehland, Y. Jia, D. G. Schlom, M. Wuttig, A. Roytburd and R. Ramesh, *Science*, 2004, **303**, 661–663.
12 F. Zavaliche, H. Zheng, L. Mohaddes-Ardabili, S. Y. Yang, Q. Zhan, P. Shafer, E. Reilly, R. Chopdekar, Y. Jia, P. Wright, D. G. Schlom, Y. Suzuki and R. Ramesh, *Nano Lett.*, 2005, **5**, 1793–1796.
13 D. Lebeugle, D. Colson, A. Forget, M. Viret, P. Bonville, J. F. Marucco and S. Fusil, *Phys. Rev. B: Condens. Matter*, 2007, **76**, 024116.
14 T. Zhao, A. Scholl, F. Zavaliche, K. Lee, M. Barry, A. Doran, M. P. Cruz, Y. H. Chu, C. Ederer, N. A. Spaldin, R. R. Das, D. M. Kim, S. H. Baek, C. B. Eom and R. Ramesh, *Nat. Mater.*, 2006, **5**, 823–829.
15 S. C. Liao, P. Y. Tsai, H. J. Liu, J. C. Yang, S. J. Lin, C. H. Lai and Y. H. Chu, *ACS Nano*, 2011, **5**, 4118–4122.
16 H. J. Liu, L. Y. Chen, Q. He, C. W. Laing, Y. Z. Chen, Y. S. Chien, Y. H. Hsieh, S. J. Lin, E. Arenholz, C. W. Luo, Y. L. Chueh, Y. C. Chen and Y. H. Chu, *ACS Nano*, 2012, **6**, 6952–6959.
17 N. M. Aimon, D. H. Kim, H. K. Choi and C. A. Ross, *Appl. Phys. Lett.*, 2012, **100**, 092901.
18 H. Zheng, Q. Zhan, F. Zavaliche, M. Sherburne, F. Straub, M. P. Cruz, L. Q. Chen, U. Dahmen and R. Ramesh, *Nano Lett.*, 2006, **6**, 1401–1407.
19 V. Skumryev, S. Stoyanov, Y. Zhang, G. Hadjipanayis, D. Givord and J. Noguès, *Nature*, 2003, **423**, 850–853.
20 I. V. Golosovsky, G. Salazar-Alvarez, A. López-Ortega, M. A. González, J. Sort, M. Estrader, S. Suriñach, M. D. Baró and J. Nogués, *Phys. Rev. Lett.*, 2009, **102**, 247201.
21 S. E. Inderhees, J. A. Borchers, K. S. Green, M. S. Kim, K. Sun, G. L. Strycker and M. C. Aronson, *Phys. Rev. Lett.*, 2008, **101**, 117202.
22 T. Burnus, Z. Hu, H. H. Hsieh, V. L. J. Joly, P. A. Joy, M. W. Haverkort, H. Wu, A. Tanaka, H.-J. Lin, C. T. Chen and L. H. Tjeng, *Phys. Rev. B: Condens. Matter*, 2008, **77**, 125124.
23 J. A. Moyer, C. A. F. Vaz, D. A. Arena, D. Kumah, E. Negusse and V. E. Henrich, *Phys. Rev. B: Condens. Matter*, 2011, **84**, 054447.
24 C. T. Chen, Y. U. Idzerda, H.-J. Lin, N. V. Smith, G. Meigs, E. Chaban, G. H. Ho, E. Pellegrin and F. Sette, *Phys. Rev. Lett.*, 1995, **75**, 152.
25 S. Xie, J. Cheng, B. W. Wessels and V. P. Dravid, *Appl. Phys. Lett.*, 2008, **93**, 181901.
26 Y. Suzuki, G. Hu, R. B. van Dover and R. J. Cava, *J. Magn. Magn. Mater.*, 1999, **191**, 1–8.
27 W. J. Antel, Jr, F. Perjeru and G. R. Harp, *Phys. Rev. Lett.*, 1999, **83**, 1439–1442.
28 H. Ohldag, A. Scholl, F. Nolting, E. Arenholz, S. Maat, A. T. Young, M. Carey and J. Stöhr, *Phys. Rev. Lett.*, 2003, **91**, 017203.
29 E. Arenholz, K. Liu, Z. Li and I. K. Schuller, *Appl. Phys. Lett.*, 2006, **88**, 072503.
30 S. Brück, S. Macke, E. Goering, X. Ji, Q. Zhan and K. M. Krishnan, *Phys. Rev. B: Condens. Matter*, 2012, **81**, 134414.
31 A. M. Mulders, H. Loosvelt, A. Fraile Rodríguez, E. Popova, T. Konishi, K. Temst, O. Karis, D. Arvanitis and C. Van Haesendonck, *J. Phys.: Condens. Matter*, 2009, **21**, 124211.
32 H. Béa, M. Bibes, F. Ott, B. Dupé, X.-H. Zhu, S. Petit, S. Fusil, C. Deranlot, K. Bouzehouane and A. Barthélémy, *Phys. Rev. Lett.*, 2008, **100**, 017204.
33 K. Ashraf and S. Salahuddin, *J. Appl. Phys.*, 2012, **111**, 103904.